5

Low Scattering Photodiode-Modulated Probe for Microwave Near-Field Imaging

Hamidreza Memarzadeh-Tehran, Jean-Jacques Laurin and Raman Kashyap
École Polytechnique de Montréal
Department of Electrical Engineering
Montreal, Canada

1. Introduction

The space surrounding a radiating or scattering object is often divided into three regions, namely reactive near-field, near-field (NF) or Fresnel region and far-field (FF) or Fraunhoffer zones. In addition, the term “very-near-field" region is sometimes defined as very close to the antenna (e.g., antenna aperture). There are no abrupt boundaries between these three zones, however there are some commonly used definitions. For antennas with a size comparable to the wavelength (λ), the NF to FF boundary is calculated as $r \approx 2D^2/\lambda$, where D is the maximum dimension of the radiating device and r is the distance between the device and observation point.
The most widespread use of near-field measurement is in antenna diagnostics. In this case, fields are sampled near the antenna, typically in the Fresnel region, and a NF-to-FF transformation is used to obtain the radiation patterns (Petre & Sarkar, 1992). Rather than extrapolating away from the antenna, another possible application consists of reconstructing the field and current on the radiating device. This may require sampling within the reactive near-field region, i.e., with $r < \lambda$. Such *in-situ* near-field diagnostics have been made on antennas (Laurin et al., 2001), microwave circuits (Bokhari et al., 1995) and device emissions (Dubois et al., 2008). They can also be used to measure the wave penetration into materials and their radio-frequency (RF) characterization purposes (Munoz et al., 2008). Dielectric properties reconstruction (Omrane et al., 2006) is another use of NF measurement. Measuring the coupling between components of microwave circuits (Baudry et al., 2007), calculating FF radiation pattern of large antennas (Yan et al., 1997), and testing for electromagnetic compatibility EMC (Baudry et al., 2007) and EMI (Quilez et al., 2008) are among the other uses of NF measurement.

1.1 Statement of the problem— Obtaining accurate NF distribution

In applications such as the source or dielectric properties reconstruction, an ill-posed inverse problem has to be solved. The solution process is highly sensitive to noise and systematic measurement error. Accurate and sensitive NF measurement systems therefore need to be designed and implemented. Typically, NF imagers suffer from three important issues: limited accuracy and sensitivity, long measurement durations and reduced dynamic ranges, all of which depend on the measuring instruments and components used.

1.2 Modulated Scatterer Technique (MST)—An accurate approach for NF imaging

The distribution of near fields can be acquired using a *direct* (Smith, 1984) or an *indirect* (Bassen & Smith, 1983) technique. In the *direct* methods a measuring probe connected to a transmission line (e.g., coaxial cable) scans over the region of interest. The transmission line carries the signals picked-up by the probe to the measurement instruments. The major drawback associated with such technique is the fact that the fields to be measured are short-circuited on the metallic constituents of the transmission line. Multiple reflections may also occur between the device under test (DUT) and the line (Bolomey & Gardiol, 2001) resulting in perturbed field measurement. Moreover, flexible transmission lines such as a coaxial cables, which are widely used in microwave systems, do not always give accurate and stable magnitude and phase measurements (Hygate, 1990). This phenomenon in turn leads to inaccurate measurement, particularly where the measuring probe has to scan a large area. In contrast, *indirect* methods (Justice & Rumsey, 1955) are based on scattering phenomenon and require no transmission lines. Instead, a scatterer locally perturbs the fields at its position and the scattered fields are detected by an antenna located away from the region of interest, so as to minimize perturbation of the fields. This antenna could be the DUT itself (i.e., monostatic mode, in which case the signal of interest appears as a reflection at the DUT's input port) or an auxiliary antenna held remotely (i.e., bistatic mode). The variations of the received signals induced by the scatterer are related to the local fields at the scatterer's positions and are interpreted as the field measurement (magnitude and phase) by means of a detector. The *indirect* method employs a scatterer which is reasonably small, does not perturb the radiating device under test but is sufficiently large so that it is able to perturb the field up to the system's measurement threshold. Thus, a trade-off has to be made between accuracy and sensitivity. The *indirect* method suffers from limited dynamic range and sensitivity (King, 1978).

To overcome the drawbacks mentioned above, a technique known as the modulated scatterer technique (MST) was proposed and developed. MST was addressed and generalized by Richmond (Richmond, 1955) to remedy the drawbacks of both the *direct* and *indirect* methods. Basically, it consists of marking the field at each spatial point using a modulated scatterer, which is called the MST probe (Bolomey & Gardiol, 2001). This technique brings some outstanding advantages in the context of NF imaging such as eliminating the need to attach a transmission line to the measuring probe and improving the sensitivity and dynamic range of the measurement. From the point of view of probe implementation, tagging the field (modulation) can be done either electrically (Richmond, 1955), optically (Hygate, 1990), and sometimes, mechanically (King, 1978). Unlike optical modulation, the other modulation techniques somehow show the same disadvantages as the *direct* method. In an electrically modulated scatterer a pair of twisted metallic or resistive wires carry modulation signals to the probe. The presence of these wires may perturb the field distribution near the DUT, resulting in inaccurate measurements, whereas in an optically modulated scatterer (OMS) the modulating signal is transferred with an optical fiber that is invisible to the electromagnetic radio-frequency signal (Hygate, 1990). Thus, it can be assumed that it will only weakly influence the DUT's field distribution to be measured.

In this chapter, the design and implementation of a NF imager equipped with an array of optically modulated scatterer (OMS) probes that is able to overcome the drawbacks associated with the conventional *direct* and *indirect* methods are addressed. Additionally, a method to improve the dynamic range of the NF imager using a carrier cancellation technique is discussed.

2. Photodiode-loaded MST probe— Optically modulated scatterer

An OMS probe includes a small size antenna loaded with a light modulated component. The modulation signal is carried by an optical fiber coupled to the photoactivated component. It is switched ON and OFF at an audio frequency causing modulation on the antenna load impedance, which results in a corresponding modulation of the fields scattered by the probe. In the bistatic configuration the scattered field is received by an auxiliary antenna, as illustrated in Fig. 1. In the monostatic case the antenna under test is used to receive the modulated signal. In the following, the design and implementation of an optically modulated scatterer (OMS) is explained and discussed. Criteria for antenna type and modulator selection, tuning network design and implementation, and an OMS probe assembly will be also covered. Finally, the probe is characterized in terms of sensitivity, accuracy, and dynamic range.

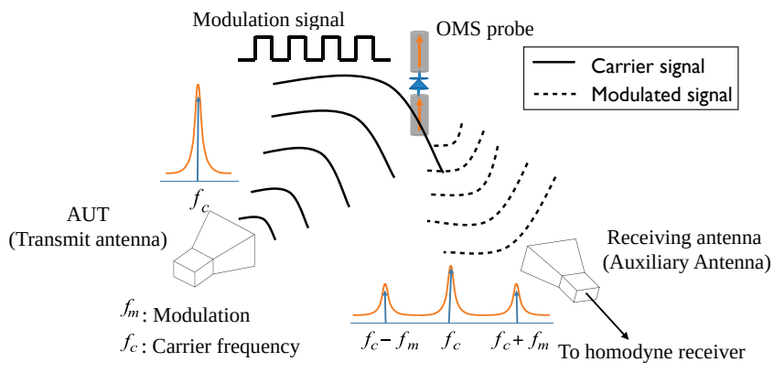

Fig. 1. Schematic of an MST-based NF imager in bistatic mode.

2.1 Antenna type

In practice, there is a limited number of antenna types that can perform as MST probes. Dipoles, loops, horns and microstrip antennas have been reported. The leading criterion to select the type of antenna is to keep the influence of the probe on the field to be measured as small as possible. The concept of a “minimum scattering antenna" (MSA) provides us with an appropriate guideline for selecting the scattering antenna. Conceptually, an MSA is invisible to electromagnetic fields when it is left open-circuited (Rogers, 1986) or connected to an appropriate reactive load (Iigusa et al., 2006). The horn and microstrip antennas do not fulfill MSA requirements due to their bulky physical structures and large ground plane, respectively, which cause significant structural-mode scattering regardless of antenna termination. The short-dipole (length$< \lambda/10$) and small-loop approach the desired MSA characteristics. A dipole probe might be a better choice because of its simpler structure. Moreover, a loop probe may measure a combination of electric and magnetic fields if it is not properly designed (King, 1978).

2.2 Modulator selection criteria

From the concept of AM modulation, we can introduce modulation index m as the ratio of the crests ($1+\mu$) and troughs ($1-\mu$) of the modulated signal envelope, where μ is the level of AM-modulation (King, 1978). Therefore, m can be defined as:

$$m = \frac{crest - trough}{crest + trough} \tag{1}$$

Assuming two states of the modulator with load impedance Z_{ON} and Z_{OFF}, and a probe impedance Z_p=Z_{dipole}+Z_{tn}, where Z_{tn} stands for the tuning network impedance[1], the modulation index of the signal scattered by the probe is given by (King, 1978):

$$m = \frac{|Z_p + Z_{ON}| - |Z_p + Z_{OFF}|}{|Z_p + Z_{ON}| + |Z_p + Z_{OFF}|} \tag{2}$$

whereas the ratio of the currents flowing in the probe terminals in both states is given by:

$$CR \equiv \frac{|I_{ON}|}{|I_{OFF}|} = \frac{|Z_p + Z_{OFF}|}{|Z_p + Z_{ON}|} \tag{3}$$

We can thus write:

$$m = \frac{1 - CR}{1 + CR} \tag{4}$$

If a small resonant probe is used, the real and imaginary parts of Z_p can be made very small, and possibly negligible compared to Z_{ON} and Z_{OFF}, such that:

$$m \approx \frac{|Z_{ON}| - |Z_{OFF}|}{|Z_{ON}| + |Z_{OFF}|} \qquad CR \approx \frac{|Z_{OFF}|}{|Z_{ON}|} \tag{5}$$

The maximum possible magnitude of the modulation index occurs when $CR = 0$ ($m = 1$) or $CR \to \infty$ ($m = -1$). Ideally, it is desired to maximize $|m|$ in order to have the strongest possible sideband response for a given level of a measured field. The selected modulated load should have either $|Z_{ON}| \gg |Z_{OFF}|$ or $|Z_{OFF}| \gg |Z_{ON}|$. In other words, input impedance of the device in the ON and OFF states should differ significantly. The results that will be presented in the next sections were obtained with probes based on a photodiode manufactured by Enablence (PDCS30T). This device was selected due to its high impedance variation as a function of input light level at a target test frequency of 2.45 GHz. The input impedance of the photodiode was measured on a wafer probing station using a calibrated Agilent 8510C vector network analyzer for different optical power levels (no light, and with a sweep from -10 dBm to 13 dBm) in the 2-3 GHz frequency range. The optical power in this measurement, was applied to the photodiode via an optical fiber, which was held above its active area by an accurate x-y positioning device.

Fig. 2a shows the impedance magnitude, revealing saturation for light power greater than +6 dBm (NB. In this figure we use the following definition $dB\Omega \equiv 20log_{10}\Omega$). The impedance of the diode in the "no-light" or OFF state and +6 dBm or ON state is shown in Fig. 2b. The diode can be modelled approximately by a series RC circuit, with $R_{OFF} = 38.8\Omega$ and $C_{OFF} = 0.31pF$. In the ON state, a similar model with $R_{ON} = 15.8\Omega$ and $C_{ON} = 13.66pF$ can be assumed. These models are approximately valid in a narrow frequency band centered at 2.45GHz. According to Equation 3, at 2.45 GHz these measured data lead to CR=13.38 (22.5 dB) and $m = -0.86$.

[1] It is assumed that this network consists of a series reactance in this example but other topologies are of course possible.

It is worth mentioning that the model used for this photodiode (i.e., series RC connection), it is only valid for small-signal operation. The photodiode switch-ON and breakdown voltages are 1.5 V and 25 V respectively. In addition, the maximum optical power should not exceed 10 dBm to prevent nonlinear operation.

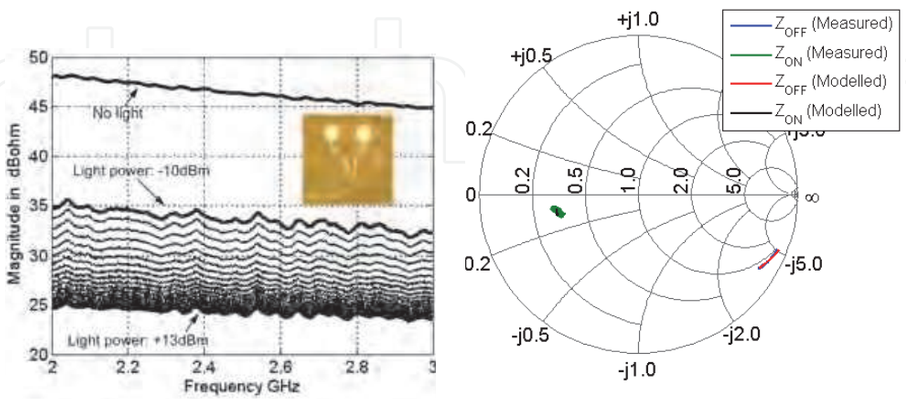

(a) (b)

Fig. 2. (a) Input impedance magnitude of the photodiode (PDCD30T manufactured by Enablence), and (b) Input impedance (normalized to 50Ω) of the photodiode chip in the 2-3 GHz range with and without illumination. The measurement results and those obtained with a model of the photodiode are compared.

2.3 Selection of OMS probe length

Usually, the scatterer (i.e., OMS probe) should have minimum interaction with the source of the fields to be measured. The dynamic range of the measurement system depends on the minimum and maximum field levels the probe is able to scatter, and the detection threshold and saturation level of the receiver. Achieving a high dynamic range necessitates using a larger scatterer at the expense of oscillations in field measurements and deviation from the true field. In general for electrically small probes, the smaller the dimension of the scatterer the smaller the expected disturbance, but at the cost of lower sensitivity. Smaller probes also lead to better image resolution. Thus, a trade-off has to be made between the dynamic range on one side and the resolution and sensitivity of the probe on the other side. The first MST dipole probe reported by Richmond (Richmond, 1955) had a length of 0.31λ. Liang et al. used a length ranging between 0.05λ-0.3λ in order to make fine and disturbance-free field maps (Liang et al., 1997). Measured electromagnetic fields were also reported in (Budka et al., 1996) for operation in the 2-18 GHz band using MST probes that are 150 μm, 250 μm, and 350 μm long. A length of 8.3 mm was used by Hygate (Hygate, 1990) for signals below 10 GHz. Nye also used 3 mm and 8 mm MST probes at f=10 GHz to obtain NF maps of antennas or any passive scatterers (Nye, 2003). The probe presented here has a length of $\lambda/12$ at a design frequency of 2.45 GHz. The impedance of the printed short dipole at this frequency, as obtained by method of moment, is $Z_p = 1.22 - j412\Omega$.

In order to ensure that a $\lambda/12$ dipole probe not only meets the requirements of MSA but also has a negligible influence on the field to be measured, let us consider the measurement

mechanism by MST probe using a network approach, as demonstrated in Fig. 3. The AUT in this figure acts as a radiating source and also a collecting antenna (i.e., port #1), and the scatter represents a measuring probe which is loaded with Z_L at port #2 (e.g., input impedance of the modulator) (King, 1978). Using of the impedance matrix of the passive network we can write:

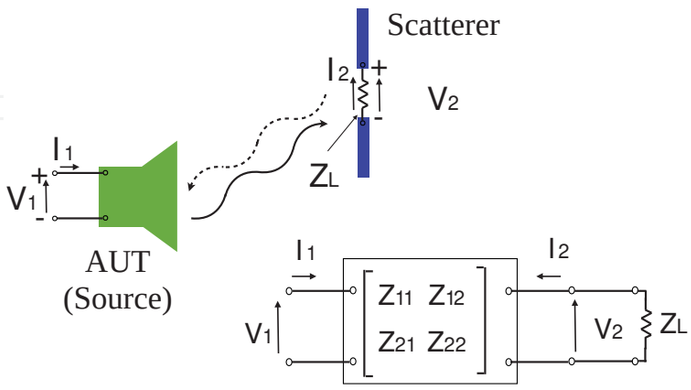

Fig. 3. Modelling of measurement mechanism using network approach, monostatic implementation.

$$V_1 = Z_{11} I_1 + Z_{12} I_2 \tag{6}$$

$$V_2 = Z_{21} I_1 + Z_{22} I_2 \tag{7}$$

The current induced in the probe (i.e., I_2) yields a voltage $V_2 = -I_2 Z_L$ on port 2. One can obtain Equation 8 by solving Equation 7 for V_1:

$$V_1 = \left(Z_{11} - \frac{Z_{12} Z_{21}}{Z_{22} + Z_L} \right) I_1 \tag{8}$$

It is also assumed that the voltage on port 1 in the absence of the scatterer is given by $V_1^0 = Z_{11}^0 I_1$, where Z_{11}^0 is the input impedance of the AUT. Then, by subtracting it from Equation 8, it yields,

$$V_1 - V_1^0 = \Delta V_1 = \left[(Z_{11} - Z_{11}^0) - \frac{Z_{12} Z_{21}}{Z_{22} + Z_L} \right] I_1 \tag{9}$$

It has been assumed that current I_1 fed to the AUT is unchanged in the two cases. Based on Equation 9, it can be shown that the measuring probe has two separate effects at the receiver's voltage, namely, the effect due to its physical structure (i.e., structural mode) and its loading (i.e., antenna mode). On the right hand side, the first term is present even when the probe is left open-circuited (i.e., when $Z_L \to \infty$), that results from the probe's structural mode. The second term appears when the probe loading (i.e., Z_L) is finite or zero, allowing current to flow in port 2. This contribution is therefore called the antenna mode. Only the latter term is modulated in MST-based probes. The first term is present and varies when the probe is moved from one measurement point to another but those variations are slow compared to the rate of modulation. It can thus be assumed that they will not affect the measurement at the modulation frequency. By considering an open-circuited scatterer (i.e., $Z_L \to \infty$), ΔV_1

gives $(Z_{11} - Z_{11}^0)I_1$; this represents the variation of the induced voltage across the AUT's terminal compared to the case in absence of the scatterer. Ideally, it is expected that ΔV_1 will vanish for MSA antennas, i.e., structural mode radiation is vanishingly small. Now, in order to

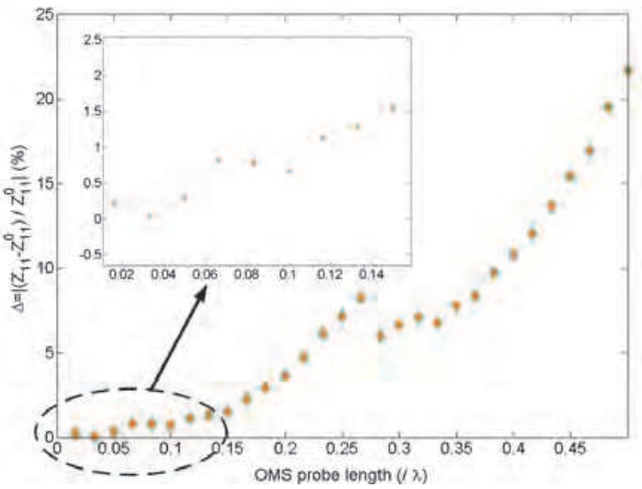

Fig. 4. AUT impedance variation due to the probe structural modes, as a function of the probe length.

investigate whether the chosen length (i.e., $\lambda/12$) for the OMS probe fulfills the requirements of the MSA antenna, we performed a simulation in Ansoft HFSS, a 3D full wave finite element solver, wherein, a planar dipole with a length of $L = 10mm$, width of $w = 1mm$ and a center gap of $g = 100\mu m$ was considered. The dipole was positioned in front of the aperture of a horn antenna operating at a test frequency of 2.45 GHz. Then, the value of $\Delta = \frac{Z_{11} - Z_{11}^0}{Z_{11}^0}$ versus the length for probe was calculated. The results plotted in Fig. 4 show that Δ varies by less than 1.5% for probes shorter than 0.15λ. Therefore, an OMS probe consisting of a short dipole with length of $\lambda/12$ can be considered as a good MSA when it is used to characterize this horn antenna.

2.4 Tuning network design

As shown in (King, 1978), scattering by the probe can be increased by adding an inductive reactance in series with the capacitive short-dipole (i.e., $Z_p = Z_{dipole} + j\omega L$) so that a resonance occurs in one of the two states. The inductance value should be chosen such that the numerator or the denominator in Equation 3 is minimized, leading to an increased modulation index. This effect, however, is frequency selective.

The value of the inductance should make the loaded short dipole resonant when the light is ON (denominator of Equation 3 minimized) and increase its impedance when the light is OFF (or vice versa). To find the optimum inductance value, one may try to maximize CR. Fig. 5 represents CR versus inductance. The inductance of 25 nH associated with the peak in the curve is referred to as the optimal point of the tuning network and it can be seen that the maximum CR is close to the estimated value 22.5 dB calculated in Section 2.2. The minimum of CR near $L = 42nH$ also leads to a local maximum of $|m|$ but it is not as high.

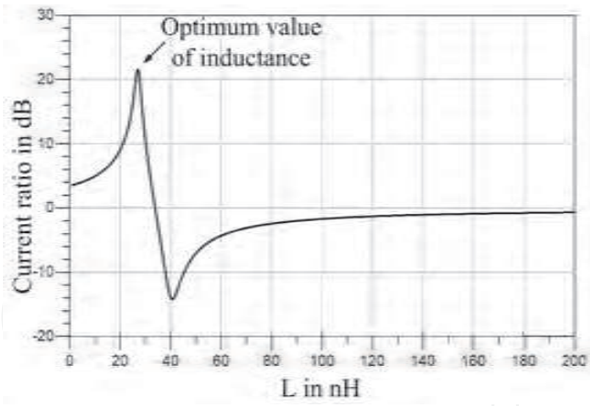

Fig. 5. Current ratio versus the inductance value used for tuning.

3. Matching network impact on the OMS probe performance

The impact of the tuning network on the probe performance is presented here. The difference between the scattered field when the dipole is in ON and OFF states (i.e. $Z_{OFF} = 38.8 - j206.2\Omega$ and $Z_{ON} = 15.9 - j4.8\Omega$) at 2.45 GHz was calculated versus frequency for two cases: with and without considering a tuning network in an OMS probe structure. To do this, a method of moment code was developed to calculate the ON and OFF states scattered field in the 1-4 GHz frequency range.

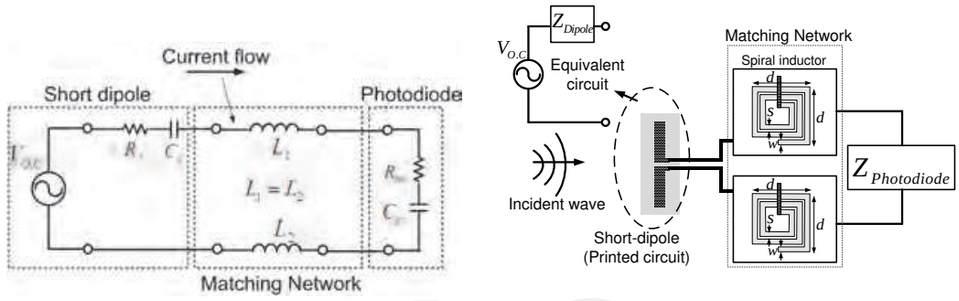

Fig. 6. (a) Schematic depicting the equivalent circuit of the OMS probe, wherein $R_d = 1.22\ \Omega$, $C_d = 0.15\ pF$, $R_p(ON) = 15.85\ \Omega$, $C_p(ON) = 13.65\ pF$, $R_p(OFF) = 38.78\ \Omega$, $C_p(OFF) = 0.31\ pF$ and $L1 = L2 = 12.7\ nH$, and (b) Matching network for the proposed OMS probe (d=0.99 mm, s=63.5 μm and w=50.8 μm). Dipole length: 1 cm. Drawing is not to scale.

In this model (see Fig. 6a), the scattered field was calculated 1 cm away from the dipole when a uniform plane wave illumination is considered. The results shown in Fig. 7 exhibits a significant improvement of about 23 dB in scattered field when the tuning network is added. As a consequence, the sensitivity of the OMS probe is significantly improved. The two peaks on the solid curve correspond to resonances that occur in the ON and OFF states of the OMS probe.

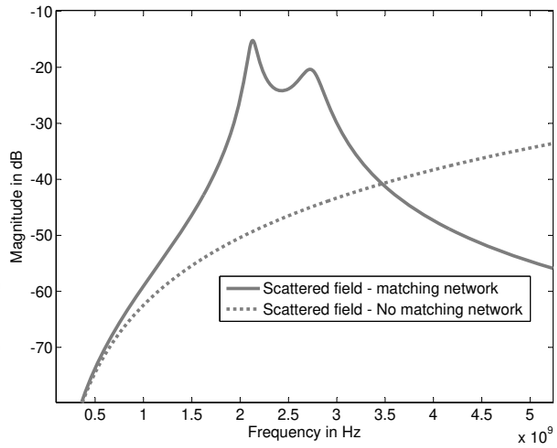

Fig. 7. Frequency response of an OMS probe: Solid line probe with tuning network and dashed line probe without tuning network.

4. OMS probe fabrication

The OMS probe was fabricated on a thin ceramic substrate (alumina) with a thickness of 250 μm, a relative permittivity of 10.2 and $tan\delta = 0.004$. An optical fiber is coupled to the active surface of the photodiode using a precision positioning system by monitoring photo-induced DC current while the fiber is moved to find the optimal position. Finally, the fiber is permanently fixed by pouring epoxy glue when in the position corresponding to the current peak. In addition, in order to prevent any damage to the coupling by mishandling the probe, a strain relief structure made of a low permittivity material ($\epsilon_r \approx 2.7$) is added. Fig. 8 shows the photograph of the completed probe assembly. The dimensions of the ceramic substrate are 7 mm and 15 mm. The tuning element is implemented with two spiral inductors (see Fig. 6b). Each inductor occupies an area of 1mm$\times$1mm. The photodiode area is $0.2mm^2$. Wire-bonding provides the electrical contacts between the photodiode and the inductor terminals on the substrate.

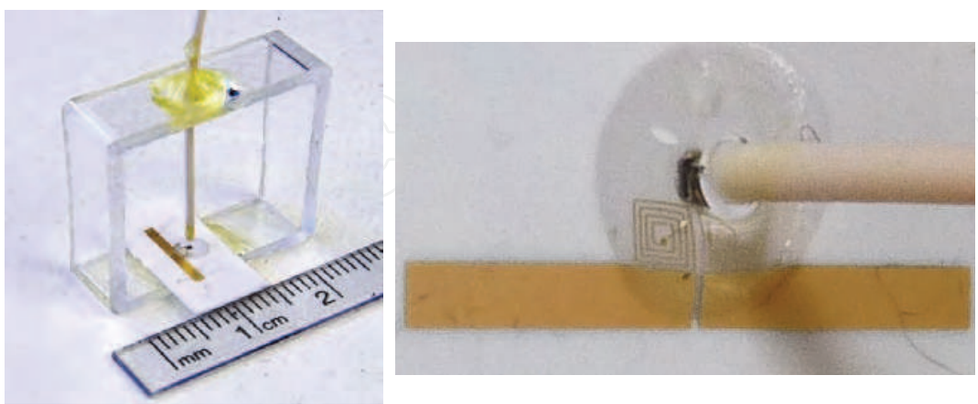

(a) 3D view (b) Top view

Fig. 8. Photograph of the implemented OMS probe.

5. Validating the fabrication process

Once the OMS probe is fabricated, including fiber coupling, it is necessary to verify whether it operates at the frequency at which it was designed. As the photodiode saturates at an input power of +6 dBm (see Fig. 2), no further modulation index change is anticipated beyond this point.

The OMS probe was tested by exposing it to a constant power electric field (e.g., near a horn antenna or microstrip transmission line) at 2.45 GHz. An optical signal (waveguide of 1.3 μm) modulated at $\sim 100 KHz$ with a power between -10 dBm to 13 dBm was applied to the OMS probe. The sidebands were recorded during this measurement at the input port of the horn using a spectrum analyzer. Fig. 9 illustrates the results obtained by this experiment. It can be seen that the level of the sidebands (normalized to its maximum) increases linearly with the optical power when it is smaller than +6 dBm. As expected, beyond this limit the probe is not able to scatter more fields. This test not only confirms that the probe is operating at a desired working point but it also shows the quality of the fiber/photodiode coupling.

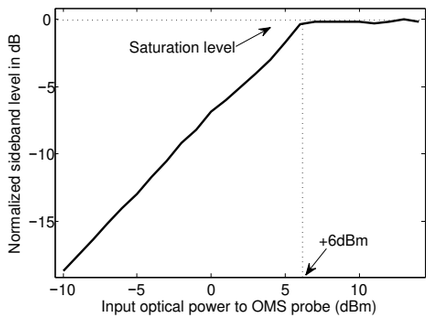

Fig. 9. Variation of sideband power level (dB) versus input optical power (dBm) to the OMS probe.

6. Omnidirectional and cross-polarization characterization

6.1 Omnidirectional response

A desirable feature for a near-field probe is to be able to measure a specific component of the E or H field. In the case of a short dipole it is the component of the E field parallel to the dipole axis, independently from the direction of arrival of the incoming wave(s). For a thin-wire dipole, rotational symmetry of the response about the dipole axis is expected. In practice the presence of a substrate, the flat strip geometry of the dipole and the presence of the dielectric support structure break the symmetry. A detailed model of the probe including these elements was simulated with Ansoft-HFSS as shown in Fig. 10a. In these simulations, the probe is on the z-axis and centered at the origin. A near-field plot of E_z (Co-pol.) and E_ϕ (Cross-pol.) on a 36 mm circle and in plane $z = 0$ are shown in Fig. 10b. The probe operates as a transmit antenna but the response in the receive mode is the same due to reciprocity. The results show a fluctuation of less than 0.45 dB in the desired E_z component, and very low level of cross-polarization.

Rotational symmetry of the response was also studied experimentally with the setup shown in Fig. 11a. In this case, the probe operates in the receiving mode and it is located near the

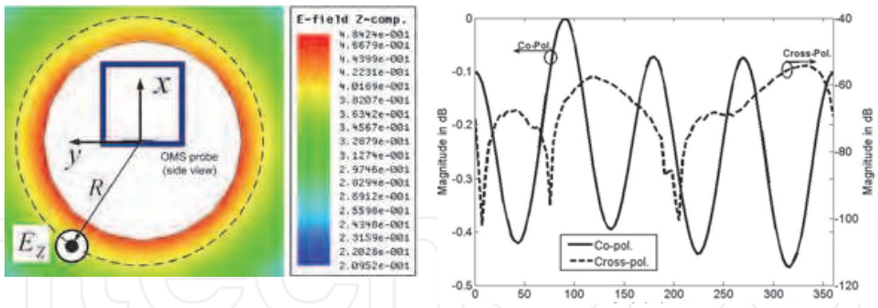

(a) Magnitude (b) Phase

Fig. 10. Schematic of the OMS probe when investigated for omnidirectivity characteristic. Co-polarized (E_z solid line) and Cross-polarization (E_ϕ dashed line) radiation of the OMS probe in the H-plane at a distance of 36 mm from the probe axis, as predicted by HFSS (the data is normalized with respect to the maximum value of E_z).

aperture of a transmitting horn antenna. The experiment was done by rotating the OMS probe about its axis while recording the power levels of the sidebands on a spectrum analyzer. The measured pattern at a distance of 12.2 cm (one free-space wavelength) shown in Fig. 11b exhibits a fluctuation of about 0.6 dB. The figure also shows simulation results obtained with HFSS. In this case, the magnitude of the difference between the horn's S_{11} parameter, in the absence and the presence of the rotated probe, is plotted. The experimental and simulated curves were normalized to make the comparison easier. In the simulation results, the effect of the dielectric substrate and support structure is barely perceptible. On the contrary, the experimental curve does not exhibit such a good rotational symmetry, as a difference of 0.6 dB can be observed between the maximum and minimum values. It is believed that this fluctuation may be due to mutual interactions between the probe rotation fixture and the horn antenna, which were not taken into account in the simulations.

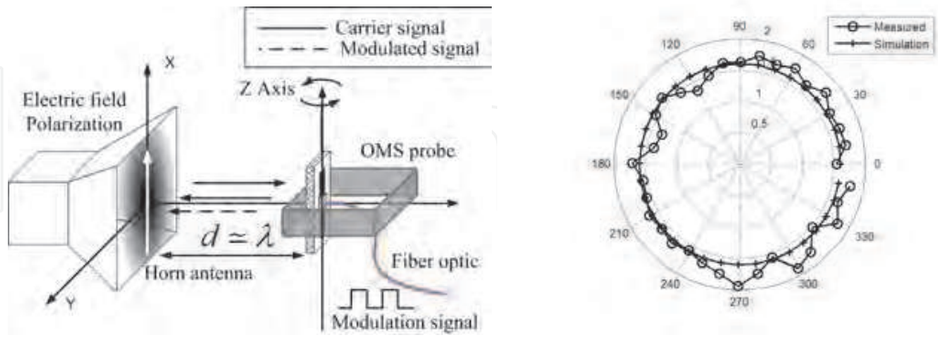

(a) (b)

Fig. 11. The setup for testing the omnidirectional performance of an OMS probe (a). Measured radiation pattern in the probe H-plane at a distance of one wavelength from the illuminating waveguide (magnitude in dB) (b).

6.2 Cross polarization

According to Fig. 10a, the cross-polarization of the OMS probe is give by Equation 10.

$$E_{\phi} = E_{cross-pol.} = -E_x \sin(\phi) + E_y \cos(\phi) \tag{10}$$

HFSS simulations predicts a cross-polarization rejection of more than 55 dB for the OMS probe. To verify this result experimentally, the coupling between two identical open-ended WR-284 rectangular waveguides that face each other (Fig. 12) was measured. Although rectangular waveguides already have very good on-axis cross-polarization rejection, it was further improved by inserting a grid of parallel metal-strips (3 strips per cm) printed on a thin polyimide substrate (thickness of 5 mil and a relative permittivity of 3.2). These polarizers were mounted on the apertures of the transmit and receive waveguides. The strips, illustrated on the Tx waveguide in Fig. 12, are oriented perpendicular to the radiated field. The Tx waveguide did not show significant change of the return-loss after adding the polarizers. In the experiment, the apertures were aligned and set one wavelength apart from each other. Then, the OMS probe was mounted on a fixture made of foam transparent to microwaves ($\epsilon_r \approx 1$) and was inserted between the aperture of the waveguide as illustrated in Fig. 12. The setup operated in a bistatic mode, i.e. the sidebands generated by the OMS probe were measured at the output port of the receive waveguide. Measurements were made with the receive waveguide rotated about its axis by 0 and 90 degrees; the level of the sidebands introduced by the probe changed by 60.55 dB. This should be considered as a lower bound on the probe-induced cross-polarization, as the cross-polarization rejection of the polarizers is not infinite in practice.

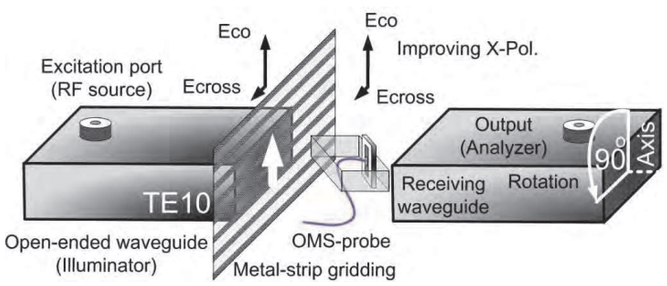

Fig. 12. Setup to measure co-to-cross polarization (E_{ϕ}) rejection of the OMS probe (only one of the polarizer sheets is shown for clarity).

7. OMS probe frequency response

The frequency response of the OMS probe was assessed by using it in a monostatic scheme. The probe was inserted in a rectangular WR-284 rectangular waveguide and aligned with the main component of the E-field. With the photodiode in the OFF state, the waveguide was connected to a calibrated vector network analyzer through a 3-stub tuner that was adjusted to give the minimum possible reflection coefficient (less than -65 dB) over the tested frequency band. Then, an optical power level of +6 dBm was applied to drive the photodiode in the ON state. The difference between the complex reflection coefficient at the tuner's input port in both states was then normalized to have the maximum at 0 dB. The results displayed in Fig. 13 show two peaks. It is believed that they are due to the different resonance frequencies of $Z_p +$

Z_{ON} and $Z_p + Z_{OFF}$ (see Fig.7). In fact, if a simple capacitor model is assumed for the short dipole in free-space, resonance frequencies of 2.53 GHz and 3.09 GHz can be calculated for the ON and OFF states respectively. Results from a simulation done with the thin-wire method of moment are also shown in the figure. In the simulation, the probe is illuminated with a uniform plane wave in free space. This shows the normalized difference between the squared scattered field taken 1 cm away from the dipole in the two states. The results also exhibit a double peak response. In the measurement, the resonance observed in the waveguide are shifted to lower frequencies. This shift is thought to be due to imperfections in the construction and uncertainty in the substrate's constitutive material parameters. Furthermore, the value of Z_p in free-space is not the same as in the waveguide where the dipole is interacting with the metallic walls. Finally, as these reflection differences are obtained by subtracting very similar measured values, the results are susceptible to measurement and simulation inaccuracies. Both curves exhibits a maximum sensitivity near the design frequency of 2.45 GHz. Finally, the waveguide measurement process described above was simulated in HFSS. The reflection coefficient difference shown in Fig. 13 exhibits peaks near 2.7 GHz and 3 GHz. It should be noted that this curve is derived from differences between S_{11} values with a variation smaller than 5×10^{-5} in magnitude. Therefore, the frequency shift compared to the other two curves may be partly due to simulation inaccuracies.

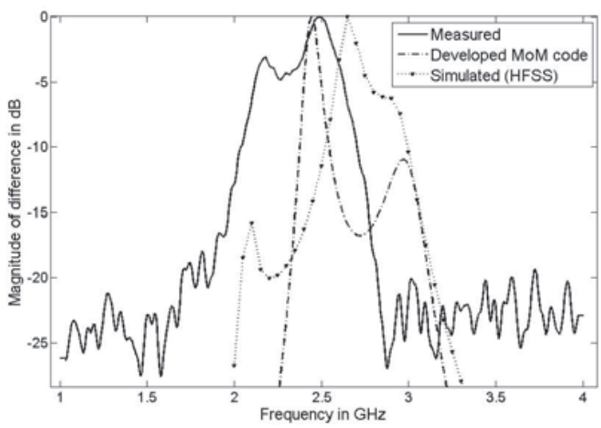

Fig. 13. Difference of frequency response for the OMS probe in ON and OFF states: solid line is the measured reflection coefficient; dashed line is the simulated scattered field; dotted line is simulated reflection coefficient.

8. OMS probe performance validation

In order to verify the performance of the developed OMS probe, it was set to measure the electric field distribution near a 50-Ω microstrip transmission line. The test was made in a monostatic setup, where the measured signal is proportional to the square of the complex electric field ($v \propto E^2$). The transmission line was fabricated on a Rogers substrate (RO3035) with a relative permittivity of 3.8 and a thickness of 60 mils (Fig. 14).

The rapidly varying fields near the line are highly suitable to assess the resolution and the dynamic range of the measurement system. In this measurement, the probe is scanned across the microstrip line at a height of 3 mm above it, and measures the transverse electric field

distribution along x (i.e., E_x) (Fig. 14). The transmission line was terminated with a matched load.

To validate the measurement results, we also included the field distribution of the transmission line predicted by HFSS (Fig. 15).The results obtained from simulation need to be post-processed to take into account the effect the finite length of the measuring probe. This topic will be discussed in Section 9.

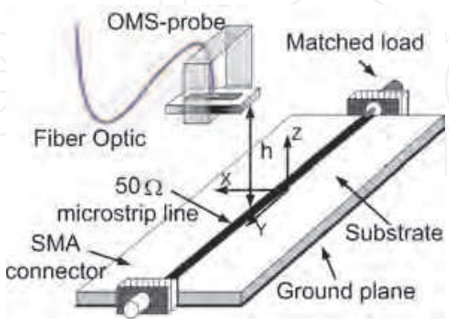

Fig. 14. Schematic of the probe and microstrip transmission line under test.

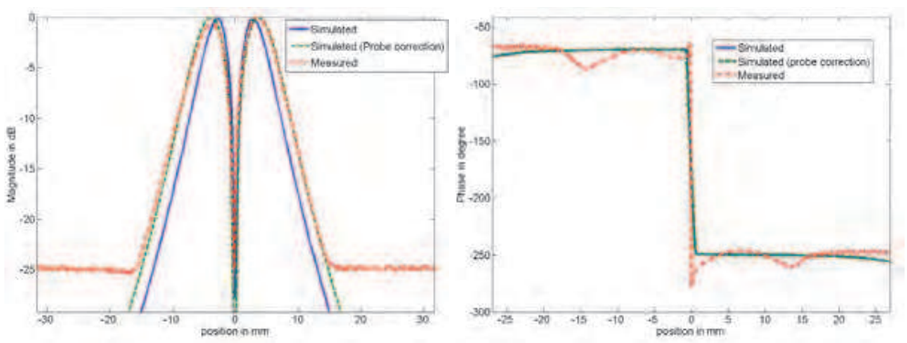

(a) Magnitude (b) Phase

Fig. 15. Measurement results and simulations (magnitude and phase) of electric field (E_x) at h =3mm.

8.1 Taking the square root: sign ambiguity removal

When the NF imager operates in monostatic mode, the measured fields are obtained by taking the square root of the measured data. The square root of a complex signal $v = X_I + jX_Q$ has two solutions and it is necessary to select the proper one. The procedure might be straightforward when the measured field takes nonzero values. In this case it is possible to ensure continuity of the phase distribution in the whole data set. In contrast, sign retrieval is not an easy task if nulls occur (i.e., $E = 0$) at some locations. In these cases, no clear method has been addressed to choose the sign of the square root correctly. However, a technique was reported in (Hygate & Nye, 1990) for some particular cases.

In the case of the microstrip line considered here it is well known that transverse electric field (E_x in Fig. 14) has a null on the strip's symmetry plane and a different sign on both sides. Thus, even if choosing the sign of the electric field on either side is impossible without *a priori*

knowledge. It is assumed that when a contour with zero E field is crossed, the phase changes by π.

9. Probe correction

The short dipole implementing the probe has a finite length. Therefore, the measured data is not representative of the fields at a point but rather of the integral of the weighted field along the probe. To take this effect into account, we used the induced *e.m.f* method for calculating the induced voltage across the probe's terminal generated by an incident E-field (see Fig. 16a). In this method, we need to know the current distribution (J) on the probe when it is radiating, i.e., acting as a transmitting antenna. Since the length of the probe is shorter than 0.1λ, one can assume that J can be approximated by triangular current distribution, as shown in Fig. 16b.

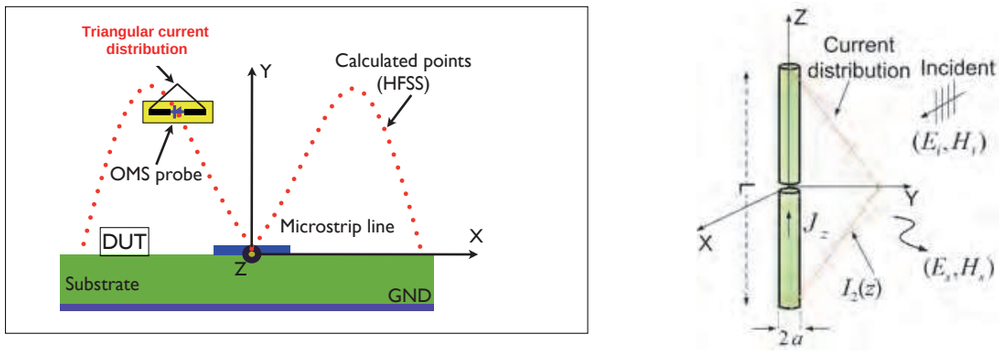

(a) (b)

Fig. 16. (a) Schematic showing the effect of a probe length on the field to be measured, and (b) Geometry for calculating the induced current on the OMS probe.

$$J_{probe} = J_{probe}(0)\left[1 - \frac{2|z|}{L}\right]u_z \tag{11}$$

The measured field is given by the field-current convolution for every point using Equation 12 (see Fig. 16b).

$$V_{probe} = -\frac{1}{J_{probe}(0)}\int_L \bar{E}_i.u_z J(z)dl \tag{12}$$

This equation was used to process the field calculated by HFSS in Fig. 15. The simulations, after applying convolution, probe correction, are in very good agreement with the measurements, both in magnitude and in phase plots, which proves the excellent performance of the probe (see Fig. 15). Within the ± 15 mm interval, the average difference between the simulated (with probe correction) and measured fields was 6.4% in magnitude and 3.2 degrees in phase. It is worth mentioning that the probe correction does not alter phase information in this example due to uniformity of the phase on both sides of the x=0 plane.

10. Sensitivity

The sensitivity of the measurement system is not only dependent on the modulation index of the loaded probe but also on the sensitivity and noise floor of the receiving equipment measuring the sideband signal. In the monostatic configuration, the magnitude of this signal is proportional to $\Delta\rho$, the difference in the AUT reflection coefficient in the photodiode's ON and OFF states. It can be proven that for a monostatic test configuration this difference is proportional to S_{21}^2 (Equation 13), where S_{21} represents coupling between the AUT and probe ports (Fig. 17) (Bolomey & Gardiol, 2001).

$$\Delta\rho \propto S_{21}^2 \rightarrow \Delta_\rho = K_1 S_{21}^2 \tag{13}$$

Furthermore, the field incident on the probe is proportional to S_{21}, i.e.,

$$E \propto S_{21} \rightarrow E = K_2 S_{21} \tag{14}$$

Using Equations 13 and 14, we can obtain:

$$E = K\frac{\Delta\rho}{S_{21}} \tag{15}$$

The sensitivity of the system to electric field can be given in terms of the minimum possible reflection coefficient that can be accurately measured, namely $\Delta\rho_{min}$. Consequently, the sensitivity of the system is simply given by

$$E_{min} = |K\frac{\Delta\rho_{min}}{S_{21}}| \tag{16}$$

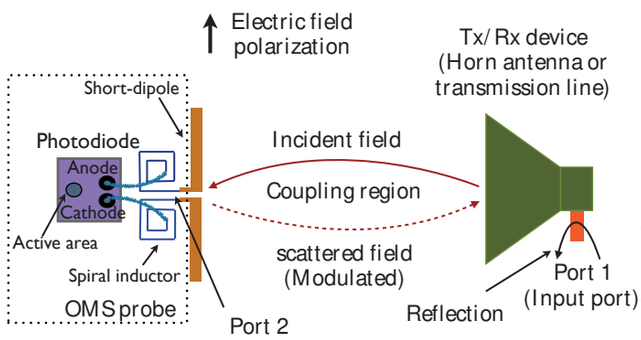

Fig. 17. Drawing of the setup used to measure sensitivity of the OMS probe.

where $K = K_2/K_1$ is a constant. The field sensitivity will therefore depend on the AUT. For a radiating structure, we expect a higher value of S_{21} and therefore a better sensitivity, than for a guiding structure such as a microstrip line. To illustrate this, we have estimated the sensitivity for two structures: a horn antenna operating at 2.45 GHz and the microstrip line terminated with a matched load. By simulation, we obtained the field incident on the probe for an incident input power of 1 watt at the DUT's input port. The same configuration was then repeated experimentally, that is to say with the probe located at the same point as in the

simulations. With the probe in this fixed position to keep S_{21} constant, the incident power was reduced with an attenuator until the receiver's noise floor was reached. The field sensitivity was then calculated by scaling the E-field value obtained in simulations by the square root of the threshold power level (in watts) measured experimentally. In the case where the probe was in the aperture of the horn (large S_{21}), the sensitivity was 0.037 V/m. When it was at a height of 3 mm above the microstrip line (small S_{21}), the sensitivity degraded to reach 54.3 V/m. This large difference illustrates a weakness of the monostatic configuration for characterizing non-radiating structures.

11. Optically modulated scatterer (OMS) probes array: Improving measurement speed in a NF imager

A linear array of seven OMS probes was developed in order to improve the measurement speed of the NF imager. In the array, the probes are laid in parallel along a line perpendicular to the probes' axes (see Fig. 18). The probes were mounted on a piece of planar foam ($\varepsilon_r \approx 1$) with a spacing of 3 cm between the probes. The foam has a thickness of 1.2 cm and is very rigid. It also prevents the array from vibrating when a very fast measurement is made. The array is moved mechanically along one direction, while being moved electronically (as well as mechanically if finer measurement resolution is required) in the orthogonal direction so as to scan a $2D$ grid. Thus, this arrangement divides by seven the number of mechanical movements in only one direction. It is shown in (Cown & Ryan, 1989) that not only the probe translations by the positioning system but also the switching time between the probes remarkably slow down scanning of the NF imager. Thus, to achieve faster measurements it is necessary to pay attention to both aspects simultaneously.

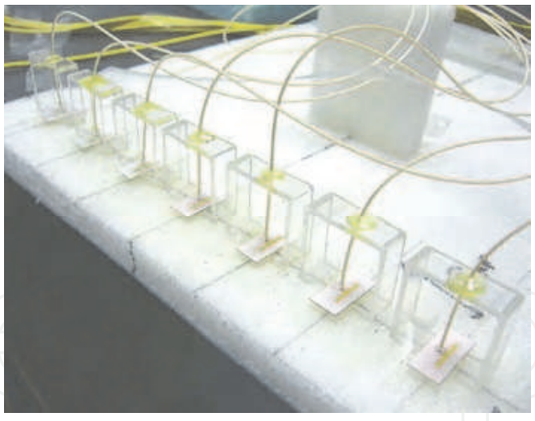

Fig. 18. Photography of the developed array of seven OMS probes.

11.1 Laser diodes array: custom-designed optical switch

In practice, it is necessary to use an optical switch in order to send a modulation signal to the designated probe in the array.

To this end, an array of controlled laser diodes (see Fig. 19) was designed and developed. Each laser diode is individually connected to a probe. A digital controller was also implemented to provide proper signaling to the probe. The controller produces a reference signal used by the

lock-in amplifier (LIA). The stability of this reference prevents phase jitter in the measured data.
The electronically switched feature of the array not only increases the measurement speed but also eliminates cross-talk between the outputs, which was observed with a mechanical optical switch. As a result, we obtained a 14-times improvement in the measurement time compared to the setup reported in (Tehran et al., 2009).

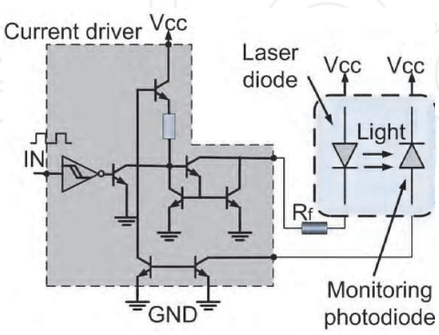

Fig. 19. Schematic showing a laser diode and its driver.

11.2 The developed NF imager equipped with array of OMS probes

Fig. 20 demonstrates the NF imager incorporating all of its essential parts namely, microwave electronic, and optical circuitries necessary to transmit/receive and process the scattered fields by an OMS probe in the NF imager. The microwave part consists of an RF source, an active circuit equivalent to a conventional I-Q demodulator and a carrier canceller circuit. Base-band analog and digital parts include a lock-in amplifier (LIA), model SR830 manufactured by Stanford Research Systems, which provides signal vector measurement (magnitude and phase), a current driver exciting and controlling a laser diode, and a digital controller that generates the reference signal required by an LIA and also that addresses the RF SPDT switch. This controller also sends commands to the laser diodes modulating the OMS probes. The whole setup is controlled by a computer software developed using LabView.

12. Validating the NF imager

12.1 Array calibration

It is practically impossible to make a set of identical OMS probes. Differences in the responses of the probes can be caused by differences in the photodiode characteristics, materials used, optical fiber/photodiode coupling quality and many other factors (Mostafavi et al., 2005). In order to quantify these differences in the probes, we performed a simple monostatic field probing experiment in which the seven probes are set to measure the E field at the same fixed point near a DUT. The obtained results are then used to compute a complex correction factor (CF) corresponding to each probe using Equation 17.

$$CF = \frac{E_{ref}}{E_{Probe\#i}}; i = 1,7 \tag{17}$$

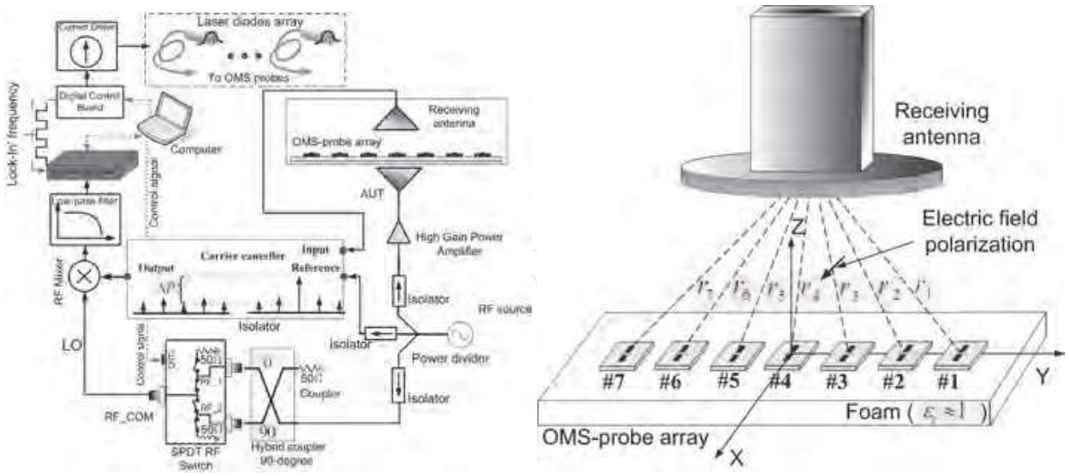

(a) Near-field imager circuitry (b) The imager receiving part

Fig. 20. (a) Near-field imager microwave circuitry configured for bistatic operation, and (b) receiving part of the imager incorporating the OMS probe array and a WR-284 rectangular waveguide.

Probe #	CF	$\|CF\|$	$\angle CF(deg)$
1	0.8704+j0.0218	0.8706	1.4347
2	0.9645-j0.0806	0.9678	4.7724
3	0.959-j0.0511	0.9603	-3.050
4	1+j0	1	0
5	1.0007-j0.0091	1.0007	-0.5210
6	1.0252+j0.0258	1.0255	1.4415
7	1.0432+j0.0406	1.0439	2.2287

Table 1. The measurement results of a known field using individual probes (all measurements have been normalized to the reading of probe #4).

In this experiment, an antenna with a highly concentrated near-field distribution was used as a DUT. This antenna incorporates a cylindrical waveguide loaded with a dielectric material having a dielectric constant about 15. This dielectric part concentrates the fields over a small area where the probe under test is located, while weakly illuminating the other probes (which are switched OFF). The probes are positioned within the illuminated region near the antenna and the fields in the E-plane of the illuminating antenna are scanned. Ideally, it is expected that the probes will measure the same field distribution. However, due to the factors mentioned earlier they do not. Therefore, as an effective compensation technique, a probe in the array is used as a reference (e.g., probe#4, central) to which the rest of the probes are weighted by a complex number (e.g., correction factor). The correction factors can be obtained for several points and averaged to get a better agreement between the responses of the probes. The computed correction factors based on the method explained here, are listed in Table 1. The effect of applying correction factors on the measurement results will be discussed later.

12.2 Receiving antenna compensation

In the bistatic test setup, the receiving part of the NF imager incorporates an auxiliary antenna (AA) to pick up the scattered fields and send them to the coherent detector, as illustrated in Fig. 20b (see also Fig. 1). During the scan, the AA is moved together with the array and its phase centre has a minimum distance from the central probe (i.e., probe#4). In this configuration, the rest of the probes are placed symmetrically on both sides of probe #4. As can be observed in Fig. 20b, the scattered fields propagate along different paths to reach the AA (i.e., r_i; i=1, 7). Each probe is also seen by the AA with a different view. Then, the picked-up signals will not be identical even if all the probes are exposed to the same fields. So, we need to compensate the measured data (raw data) for the NF radiation pattern of the AA. In principle, the simple compensation method described in the previous subsection should suffice. In practice however it has been observed that the coupling between each probe and the AA slightly varies when the probes are moved near the AUT, even if the AA is maintained at a fixed position with respect to the probe array. This variation comes from mutual interaction of the AA and probe array with the AUT, which is not constant during the scan. A method to compensate for this effect is introduced in the next paragraph. We first set the AA in Fig. 20b

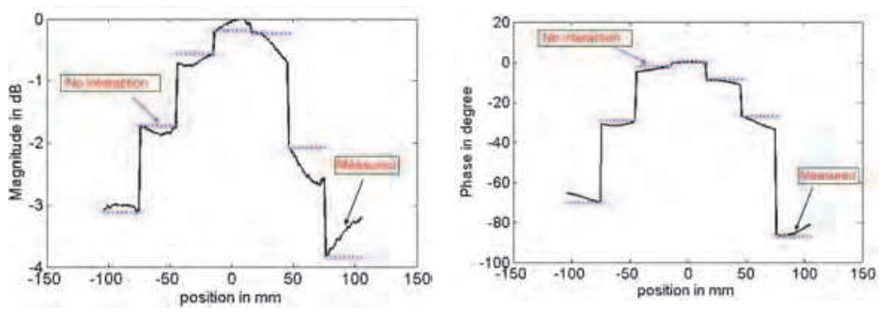

(a) Magnitude (b) Phase

Fig. 21. The measurement result obtained in the test to compensate for the radiation pattern of the receiving antenna; (a) magnitude and (b) phase of the normalized measured E field by the AA in the monostatic setup.

to operate as an illuminator in a monostatic mode (TX/RX device). During this test the AUT is passive and terminated with a matched load. In this experiment, the probes are addressed successively and then moved to a new position until the array scans the region of interest above the AUT. Ideally, a flat response is expected over the region scanned by each probe, but given the interaction of the array with the surrounding objects, including the passive AUT, and the interaction between probes, the measured results are not constant, as illustrated in Fig. 21. In this test the AUT was a horn antenna and the array was scanned at a height of 30 mm (i.e., $\lambda/4$) above the aperture. The ideal results, i.e., with no interaction between the probes with the AUT and the AA are shown by broken line in Fig. 21. The asymmetry of the curves occurs because of discrepancies in the probes of the array, displacement of probes and misalignment. Even though each probe is at a fixed distance and angle from the receiving antenna, significant variation can be observed when a 30 mm interval is scanned. The results also demonstrate the importance of the compensation before any comparison is made to validate the imager's results. After this test, the E-field measurements of the AA at each

position of the array and for each probe (i.e., E_{AA}) are used to correct the NF measurements obtained for the AUT in the bistatic setup, i.e.,:

$$E_{AUT} = \frac{E_{AUT,Bistatic}}{E_{AA}} \tag{18}$$

13. OMS probes array: validation results

The electric field distribution of a planar inverted-F antenna (PIFA, Fig. 22) radiating at 2.45 GHz was measured in bistatic and monostatic modes on a plane located at $\lambda/4$ above the antenna's ground plane (Fankem & Melde, 2008). Such an antenna is commonly used in portable devices (e.g., cellphone) and communication systems.
Fig. 23 shows 2D measurement of the AUT E-field distribution after compensation for probes' differences, receiving antenna radiation pattern and variations of interactions with the AUT. The magnitude plot shows a dynamic range of ∼25 dB over a scan area of 240 mm by 210 mm. Fig. 24 shows E- and H-planes NF cuts of the PIFA, including the measured magnitude and phase. For validating the results obtained by the imager, all measurements are compared with simulations and also to the field distribution obtained by the imager operating in the monostatic mode. All curves (i.e., magnitude of E-field) are in good agreement with each other except that of the monostatic measurement, which deviates from the true field starting from -20 mm toward negative x values.

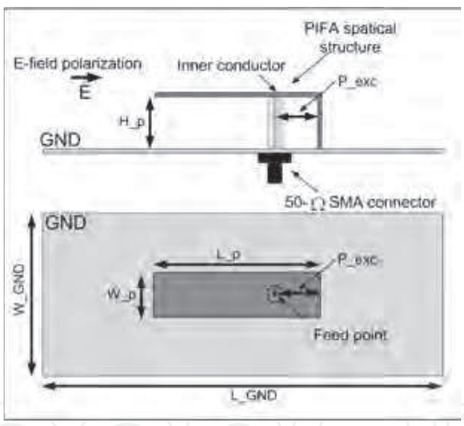

Fig. 22. Antenna under test (AUT). PIFA antenna operating at 2.45 GHz with measured return-loss of about 12 dB; the physical dimensions of the PIFA are as follows: L_p=27 mm, W_p=13 mm, H_p=7 mm, P_{exc}=7 mm, W_{GND}=70 mm and L_{GND}=137 mm.

In all cases the measured phase information in the E-plane of the PIFA are in good agreement over the whole x interval. In order to quantify the difference between the measurement results and the simulated distribution of the PIFA, the mean square error of the data was calculated. The error associated with E-plane and H-plane cuts are 0.12% and 0.06%, respectively, with respect to simulations. The benefit of probe correction in the bistatic case is clearly visible in the H-plane results.

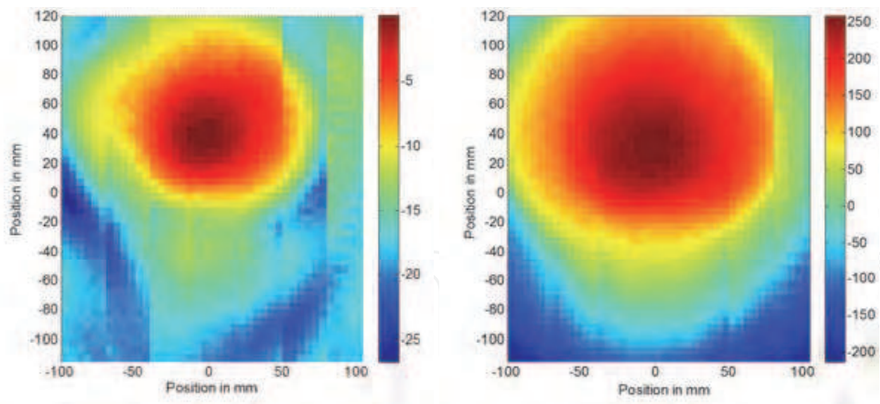

(a) Magnitude (b) Phase

Fig. 23. 2-D map of electric field distribution measured (compensated results) at a distance of $\lambda/4$ above AUT; (a) magnitude (dB) and (b) phase (deg.).

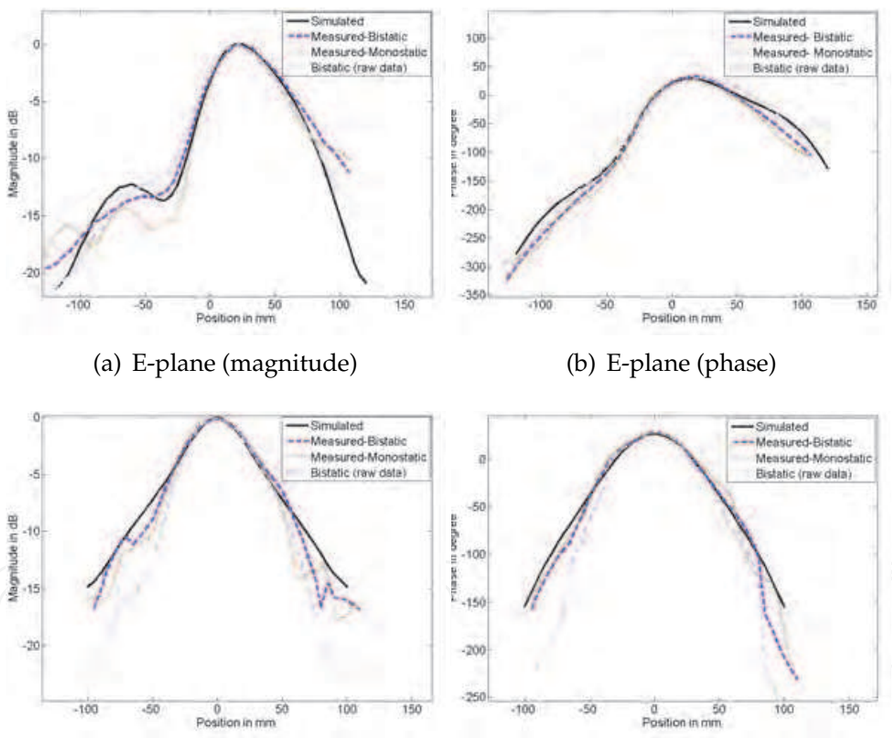

(a) E-plane (magnitude) (b) E-plane (phase)

(c) H-plane (magnitude) (d) H-plane (phase)

Fig. 24. E- and H-plane cuts of the measured E-field at distance of $\lambda/4$ from the PIFA antenna's ground plane; (a) and (c) magnitude (dB), and (b) and (d) phase (deg.).

14. Carrier cancellation: NF imager dynamic range and linearity improvement

In an MST-based NF imager the received signals (modulated) consist of a carrier and sidebands. Although the probe reflects the field at the carrier frequency, this does not affect

the measurements, which are performed at the sideband frequencies. The carrier is generally stronger (e.g., $\sim 50dB$) than the sidebands in the modulated signal. Nonlinear behaviour such as saturation and compression in the receiver occurs at higher powers of the carrier, particularly beyond -3 dBm.
To overcome these problems, the NF imager can be equipped with an automated circuit, so-called the carrier canceller, in order to eliminate the carrier from the received signals and leave the sidebands intact. This allows us to amplify the signal applied to AUTs, leading to a higher sideband level. As a consequence, the signal-to-noise (SNR) ratio of the modulated signals at the coherent detector's front-end improves considerably, resulting in larger dynamic range. The carrier at the receiving port is minimized by combining the received signal with a 180-degree out-of-phase tone at the carrier frequency whose magnitude and phase are adjusted adaptively.

14.1 High-dynamic range NF imager: Example of application

In order to demonstrate the high dynamic range of the NF imager when it is equipped with the carrier cancellation circuit, the E-field distribution above a bandpass filter operating at 2.45 GHz was measured. The measurement was performed 3 mm above the traces at 2.45 GHz. Figure 25a shows photograph of the filter under test. The results shown in Figure 25b-c include both magnitude and phase of E_x. It can be seen, that the power propagate through the filter to reach the matched load. The achieved dynamic range of the near-field map is approximately 80 dB.

15. Conclusions

This chapter addressed and discussed the design and implementation of a NF imager based on the modulated scatterer technique (MST) in detail. The imager consists of several optically modulated scatterer (OMS) probes that are very accurate, highly sensitive and also frequency selective. Each OMS probe was optimized to operate at 2.45 GHz. This probe, guarantees almost perturbation-free measurements. It can be implemented with low-cost commercial off-the-shelf photodiodes. The OMS probes were also studied and verified for omnidirectionality and cross-polarization rejection performance. The probes showed an absolute deviation of about ± 0.3 dB with respect to an omnidirectional response. The co-to-cross polarization ratio was measured and found to be better than 60 dB. The frequency response of the probe was studied theoretically and experimentally in order to qualify the performance of the matching network and to assess its impact on the frequency response of the OMS probes. The performance of the probes was validated by measuring the NF distribution of a 50 Ω microstrip transmission line. The measurements were compared with results of simulations using HFSS. The results also showed that the sensitivity of the measurement system can be as low as 0.037 V/m. Error associated with magnitude and phase measurement of respectively 6.4% and 3.2 degrees were observed. By developing a linear array of OMS probes, the measurement speed for an E-field measurement was increased more than 14 times compared to that obtained with a commercially available opto-mechanically switched systems. To improve the accuracy of measurements using the array, the raw measurement data were corrected using the proposed calibration technique, to compensate for uncertainties in the probes' responses. The E-field measurements made with the developed imager were in good agreement with the simulations and were very rapid. Benefiting from carrier

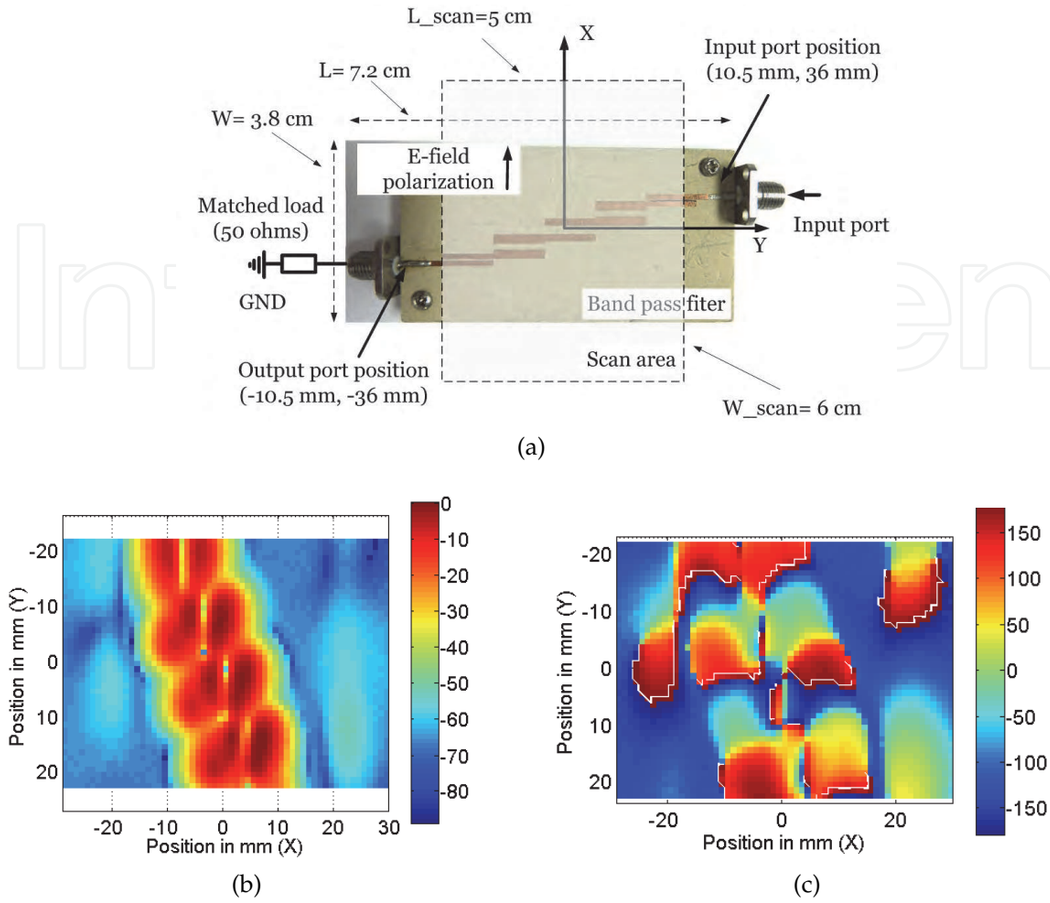

Fig. 25. The measurement results of the transverse E-field above a bandpass filter at 2.45 GHz; (a) magnitude and (b) phase.

cancellation, the isolation between the input and output ports of the imager was improved by about 60 dB. This enabled us to increase the signal fed to the NF imager and reach an overall dynamic range of 85 dB, i.e., an increase of 18 dB compared to the case when the NF imager is not equipped with the carrier cancellation circuit.

16. References

Bassen, H. & Smith, G. (1983). Electric field probes–a review, *Antennas and Propagation, IEEE Transactions on* 31(5): 710–718.

Baudry, D., Arcambal, C., Louis, A., Mazari, B. & Eudeline, P. (2007). Applications of the near-field techniques in emc investigations, *Electromagnetic Compatibility, IEEE Transactions on* 49(3): 485–493.

Bokhari, S., Zurcher, J.-F., Mosig, J. & Gardiol, F. (1995). Near fields of microstrip antennas, *Antennas and Propagation, IEEE Transactions on* 43(2): 188–197.

Bolomey, J. & Gardiol, F. (2001). *Engineering applications of the modulated scatterer technique*, Artech House.

Budka, T., Waclawik, S. & Rebeiz, G. (1996). A coaxial 0.5-18 ghz near electric field measurement system for planar microwave circuits using integrated probes, *Microwave Theory and Techniques, IEEE Transactions on* 44(12): 2174–2184.

Cown, B. & Ryan, C.E., J. (1989). Near-field scattering measurements for determining complex target rcs, *Antennas and Propagation, IEEE Transactions on* **37**(5): 576–585.

Dubois, T., Jarrix, S., Penarier, A., Nouvel, P., Gasquet, D., Chusseau, L. & Azais, B. (2008). Near-field electromagnetic characterization and perturbation of logic circuits, *Instrumentation and Measurement, IEEE Transactions on* **57**(11): 2398–2404.

Fankem, B. & Melde, K. (2008). Nested pifas for dual mode of operation: Gps and global communications, *Antennas and Wireless Propagation Letters, IEEE* **7**: 701–705.

Hygate, G. (1990). Measuring microwave fields with a minimum of perturbation, *Precision Electromagnetic Measurements, 1990. CPEM '90 Digest., Conference on*, pp. 198–199.

Hygate, G. & Nye, J. F. (1990). Measuring microwave fields directly with an optically modulated scatterer, *Measurement Science and Technology* 1(8): 703–709.

Iigusa, K., Sawaya, T., Taromaru, M., Ohira, T. & Komiyama, B. (2006). Experimental proof of electrically invisible state of inductively loaded dipole and proposal of electrically invisible meander-lines, *Antennas and Propagation, IEEE Transactions on* 54(11): 3374–3382.

Justice, R. & Rumsey, V. (1955). Measurement of electric field distributions, *Antennas and Propagation, IRE Transactions on* 3(4): 177–180.

King, R. J. (1978). *Microwave Homodyne System*, Wiley New York.

Laurin, J.-J., Zurcher, J.-F. & Gardiol, F. (2001). Near-field diagnostics of small printed antennas using the equivalent magnetic current approach, *Antennas and Propagation, IEEE Transactions on* 49(5): 814–828.

Liang, W., Hygate, G., Nye, J., Gentle, D. & Cook, R. (1997). A probe for making near-field measurements with minimal disturbance: the optically modulated scatterer, *Antennas and Propagation, IEEE Transactions on* 45(5): 772–780.

Mostafavi, M., Bolomey, J.-C. & Picard, D. (2005). Experimental study on compensation of array element pattern of collinear dipole array sensor, *EICE Trans Commun, Inst Electron Inf Commun Eng.* E88-B(8): 3314–3316.

Munoz, K., Perrey, A. & Zoughi, R. (2008). Potential application of the modulated scatterer technique to multilayered material evaluation and health monitoring, *Instrumentation and Measurement Technology Conference Proceedings, 2008. IMTC 2008. IEEE*, pp. 1643–1647.

Nye, J. (2003). A simple method of spherical near-field scanning to measure the far fields of antennas or passive scatterers, *Antennas and Propagation, IEEE Transactions on* 51(8): 2091–2098.

Omrane, B., Laurin, J.-J. & Goussard, Y. (2006). Subwavelength-resolution microwave tomography using wire grid models and enhanced regularization techniques, *Microwave Theory and Techniques, IEEE Transactions on* 54(4): 1438–1450.

Petre, P. & Sarkar, T. (1992). Planar near-field to far-field transformation using an equivalent magnetic current approach, *Antennas and Propagation, IEEE Transactions on* 40(11): 1348 –1356.

Quilez, M., Aragon, M., Atienza, A., Fernandez-Chimeno, M., Riu, P. & Silva, F. (2008). A near-field probe for in situ emi measurements of industrial installations, *Electromagnetic Compatibility, IEEE Transactions on* **50**(4): 1007–1010.

Richmond, J. (1955). A modulated scattering technique for measurement of field distributions, *Microwave Theory and Techniques, IRE Transactions on* 3(4): 13–15.

Rogers, P. (1986). Application of the minimum scattering antenna theory to mismatched antennas, *Antennas and Propagation, IEEE Transactions on* **34**(10): 1223–1228.

Smith, G. (1984). Limitations on the size of miniature electric-field probes, *Microwave Theory and Techniques, IEEE Transactions on* 32(6): 594–600.

Tehran, H., Laurin, J.-J. & Kashyap, R. (2009). A low-perturbation near-field imager equipped with optical mst probes, *Antennas and Propagation, 2009. EuCAP 2009. 3rd European Conference on*, pp. 3649–3653.

Yan, B., Saoudy, S. & Sinha, B. (1997). A low cost planar near-field/far-field antenna measurement system, *Antennas and Propagation Society International Symposium, 1997. IEEE., 1997 Digest*, Vol. 1, pp. 152–155 vol.1.

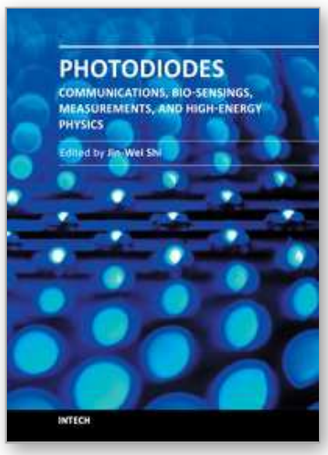

Photodiodes - Communications, Bio-Sensings, Measurements and High-Energy Physics

Edited by Associate Professor Jin-Wei Shi

ISBN 978-953-307-277-7
Hard cover, 284 pages
Publisher InTech
Published online 06, September, 2011
Published in print edition September, 2011

This book describes different kinds of photodiodes for applications in high-speed data communication, biomedical sensing, high-speed measurement, UV-light detection, and high energy physics. The photodiodes discussed are composed of several different semiconductor materials, such as InP, SiC, and Si, which cover an extremely wide optical wavelength regime ranging from infrared light to X-ray, making the suitable for diversified applications. Several interesting and unique topics were discussed including: the operation of high-speed photodiodes at low-temperature for super-conducting electronics, photodiodes for bio-medical imaging, single photon detection, photodiodes for the applications in nuclear physics, and for UV-light detection.

InTech Europe
University Campus STeP Ri
Slavka Krautzeka 83/A
51000 Rijeka, Croatia
Phone: +385 (51) 770 447
Fax: +385 (51) 686 166
www.intechopen.com

InTech China
Unit 405, Office Block, Hotel Equatorial Shanghai
No.65, Yan An Road (West), Shanghai, 200040, China
中国上海市延安西路65号上海国际贵都大饭店办公楼405单元
Phone: +86-21-62489820
Fax: +86-21-62489821

IntechOpen